



This is a repository copy of *The VLT-FLAMES Tarantula Survey*.

White Rose Research Online URL for this paper:  
<https://eprints.whiterose.ac.uk/120560/>

Version: Accepted Version

---

**Article:**

Ramírez-Agudelo, O.H., Sana, H., de Koter, A. et al. (21 more authors) (2017) The VLT-FLAMES Tarantula Survey. *Astronomy & Astrophysics*, 600. A81. ISSN 0004-6361

<https://doi.org/10.1051/0004-6361/201628914>

---

© 2017 ESO. Reproduced with permission from Astronomy & Astrophysics.

**Reuse**

Items deposited in White Rose Research Online are protected by copyright, with all rights reserved unless indicated otherwise. They may be downloaded and/or printed for private study, or other acts as permitted by national copyright laws. The publisher or other rights holders may allow further reproduction and re-use of the full text version. This is indicated by the licence information on the White Rose Research Online record for the item.

**Takedown**

If you consider content in White Rose Research Online to be in breach of UK law, please notify us by emailing [eprints@whiterose.ac.uk](mailto:eprints@whiterose.ac.uk) including the URL of the record and the reason for the withdrawal request.



[eprints@whiterose.ac.uk](mailto:eprints@whiterose.ac.uk)  
<https://eprints.whiterose.ac.uk/>

# The VLT-FLAMES Tarantula Survey★

## XXIV. Stellar properties of the O-type giants and supergiants in 30 Doradus

O.H. Ramírez-Agudelo<sup>1,2,3</sup>, H. Sana<sup>4</sup>, A. de Koter<sup>1,4</sup>, F. Tramper<sup>5</sup>, N.J. Grin<sup>1,2</sup>, F.R.N. Schneider<sup>6</sup>, N. Langer<sup>2</sup>, J. Puls<sup>7</sup>, N. Markova<sup>8</sup>, J.M. Bestenlehner<sup>9</sup>, N. Castro<sup>10</sup>, P.A. Crowther<sup>11</sup>, C.J. Evans<sup>3</sup>, M. García<sup>12</sup>, G. Gräfener<sup>2</sup>, A. Herrero<sup>13,14</sup>, B. van Kempen<sup>1</sup>, D.J. Lennon<sup>5</sup>, J. Maíz Apellániz<sup>15</sup>, F. Najarro<sup>12</sup>, C. Sabín-Sanjulián<sup>16</sup>, S. Simón-Díaz<sup>13,14</sup>, W.D. Taylor<sup>3</sup>, and J.S. Vink<sup>17</sup>

<sup>1</sup> Astronomical Institute Anton Pannekoek, Amsterdam University, Science Park 904, 1098 XH, Amsterdam, The Netherlands  
e-mail: oscar.ramirez@stfc.ac.uk

<sup>2</sup> Argelander-Institut für Astronomie, Universität Bonn, Auf dem Hügel 71, 53121 Bonn, Germany

<sup>3</sup> UK Astronomy Technology Centre, Royal Observatory Edinburgh, Blackford Hill, Edinburgh, EH9 3HJ, United Kingdom

<sup>4</sup> Institute of Astrophysics, KU Leuven, Celestijnenlaan 200D, 3001, Leuven, Belgium

<sup>5</sup> European Space Astronomy Centre (ESAC), Camino bajo del Castillo, s/n Urbanizacion Villafranca del Castillo, Villanueva de la Cañada, E-28 692 Madrid, Spain

<sup>6</sup> Department of Physics, University of Oxford, Keble Road, Oxford OX1 3RH, United Kingdom

<sup>7</sup> LMU Munich, Universitätssternwarte, Scheinerstrasse 1, 81679 München, Germany

<sup>8</sup> Institute of Astronomy with NAO, Bulgarian Academy of Sciences, PO Box 136, 4700 Smoljan, Bulgaria

<sup>9</sup> Max-Planck-Institut für Astronomie, Königstuhl 17, 69117 Heidelberg, Germany

<sup>10</sup> Department of Astronomy, University of Michigan, 1085 S. University Avenue, Ann Arbor, MI 48109-1107, USA

<sup>11</sup> Department of Physics and Astronomy University of Sheffield, Sheffield, S3 7RH, United Kingdom

<sup>12</sup> Centro de Astrobiología (CSIC-INTA), Ctra. de Torrejón a Ajalvir km-4, E-28850 Torrejón de Ardoz, Madrid, Spain

<sup>13</sup> Departamento de Astrofísica, Universidad de La Laguna, Avda. Astrofísico Francisco Sánchez s/n, E-38071 La Laguna, Tenerife, Spain

<sup>14</sup> Instituto de Astrofísica de Canarias, C/ Vía Láctea s/n, E-38200 La Laguna, Tenerife, Spain

<sup>15</sup> Centro de Astrobiología (CSIC-INTA), ESAC campus, Camino bajo del castillo s/n, Villanueva de la Cañada, E-28 692 Madrid, Spain.

<sup>16</sup> Instituto de Investigación Multidisciplinar en Ciencia y Tecnología, Universidad de La Serena, Raúl Bitrán 1305, La Serena, Chile

<sup>17</sup> Armagh Observatory, College Hill, Armagh, BT61 9DG, Northern Ireland, United Kingdom

Accepted ....

### ABSTRACT

**Context.** The Tarantula region in the Large Magellanic Cloud contains the richest population of spatially resolved massive O-type stars known so far. This unmatched sample offers an opportunity to test models describing their main-sequence evolution and mass-loss properties.

**Aims.** Using ground-based optical spectroscopy obtained in the framework of the VLT-FLAMES Tarantula Survey (VFTS), we aim to determine stellar, photospheric and wind properties of 72 presumably single O-type giants, bright giants and supergiants and to confront them with predictions of stellar evolution and of line-driven mass-loss theories.

**Methods.** We apply an automated method for quantitative spectroscopic analysis of O stars combining the non-LTE stellar atmosphere model FASTWIND with the genetic fitting algorithm PIRATA to determine the following stellar properties: effective temperature, surface gravity, mass-loss rate, helium abundance, and projected rotational velocity. The latter has been constrained without taking into account the contribution from macro-turbulent motions to the line broadening.

**Results.** We present empirical effective temperature versus spectral subtype calibrations at LMC-metallicity for giants and supergiants. The calibration for giants shows a +1kK offset compared to similar Galactic calibrations; a shift of the same magnitude has been reported for dwarfs. The supergiant calibrations, though only based on a handful of stars, do not seem to indicate such an offset. The presence of a strong upturn at spectral type O3 and earlier can also not be confirmed by our data. In the spectroscopic and classical Hertzsprung-Russell diagrams, our sample O stars are found to occupy the region predicted to be the core hydrogen-burning phase by Brott et al. (2011) and Köhler et al. (2015). For stars initially more massive than approximately  $60 M_{\odot}$ , the giant phase already appears relatively early on in the evolution; the supergiant phase develops later. Bright giants, however, are not systematically positioned between giants and supergiants at  $M_{\text{init}} \gtrsim 25 M_{\odot}$ . At masses below  $60 M_{\odot}$ , the dwarf phase clearly precedes the giant and supergiant phases; however this behavior seems to break down at  $M_{\text{init}} \lesssim 18 M_{\odot}$ . Here, stars classified as late O III and II stars occupy the region where O9.5-9.7 V stars are expected, but where few such late O V stars are actually seen. Though we can not exclude that these stars represent a physically distinct group, this behaviour may reflect an intricacy in the luminosity classification at late O spectral subtype. Indeed, on the basis of a secondary classification criterion, the relative strength of Si IV to He I absorption lines, these stars would have been assigned a luminosity class IV or V. Except for five stars, the helium abundance of our sample stars is in agreement with the initial LMC composition. This outcome is independent of their projected spin rates. The aforementioned five stars present moderate projected rotational velocities (i.e.,  $v_{\text{e}} \sin i < 200 \text{ km s}^{-1}$ ) and hence do not agree with current predictions of rotational mixing in main-sequence stars. They may potentially reveal other physics not included in the models such as binary-interaction effects. Adopting theoretical results for the wind velocity law, we find modified wind momenta for LMC stars that are  $\sim 0.3$  dex higher than earlier results. For stars brighter than  $10^5 L_{\odot}$ , that is, in the regime of strong stellar winds, the measured (unclumped) mass-loss rates could be considered to be in agreement with line-driven wind predictions of Vink et al. (2001) if the clump volume filling factors were  $f_{\text{V}} \sim 1/8$  to  $1/6$ .

**Key words.** stars: early-type – stars: evolution – stars: fundamental parameters – Magellanic Clouds – Galaxies: star clusters: individual: 30 Doradus

## 1. Introduction

Bright, massive stars play an important role in the evolution of galaxies and of the universe as a whole. Nucleosynthesis in their interiors produces the bulk of the chemical elements (e.g., Prantzos 2000; Matteucci 2008), which are released into the interstellar medium through powerful stellar winds (e.g., Puls et al. 2008) and supernova explosions. The associated kinetic energy that is deposited in the ISM affects the star-forming regions where massive stars reside (e.g., Beuther et al. 2008). The radiation fields they emit add to this energy and supply copious amounts of hydrogen-ionizing photons and  $H_2$  photodissociating photons. Massive stars that resulted from primordial star formation (e.g., Hirano et al. 2014, 2015) are potential contributors to the re-ionization of the universe and have likely played a role in galaxy formation (e.g., Bromm et al. 2009). Massive stars produce a variety of supernovae, including type Ib, Ic, Ic-BL, type IIP, IIL, IIb, IIn, and peculiar supernovae, and gamma-ray bursts (e.g., Langer 2012), that can be seen up to high redshifts (Zhang et al. 2009).

Models of massive-star evolution predict the series of morphological states that these objects undergo before reaching their final fate (e.g., Brott et al. 2011; Ekström et al. 2012; Groh et al. 2014; Köhler et al. 2015). Studying populations of massive stars spanning a range of metallicities is a proven way of testing and calibrating the assumptions of such calculations, and lends support to such predictions at very low and zero metallicity. O-type stars are of particular interest as they sample the main-sequence phase in the mass range of  $15 M_\odot$  to  $\sim 70 M_\odot$ . They show a rich variety of spectral subtypes whether dwarfs, giants, or supergiants (e.g., Sota et al. 2011), emphasizing the need for large samples to confront theoretical predictions.

To constrain the properties of massive stars, high-quality spectra and sophisticated modeling tools are required. In recent years, several tens of objects have been studied in the Large Magellanic Cloud (LMC) providing and initial basis to confront theory with observations. Puls et al. (1996) included six LMC objects in their larger sample of Galactic and Magellanic Cloud sources, pioneering the first large-scale quantitative spectroscopic study of O stars. Crowther et al. (2002) presented an analysis of three LMC Oaf+ supergiants and one such object in the Small Magellanic Cloud (SMC) using far-ultraviolet FUSE, ultraviolet IUE/HST, and optical VLT ultraviolet-visual Echelle Spectrograph data. Massey et al. (2004, 2005) derived the properties of a total of 40 Magellanic Clouds stars, 24 of which are in the LMC (including 10 in R136) using data collected with Hubble Space Telescope (HST) and the 4m-CTIO telescope. Mokiem et al. (2007a) studied 23 LMC O stars using the VLT-FLAMES instrument, of which 17 are in the star-forming regions N11. Expanding on their earlier work, Massey et al. (2009) scrutinized another 23 Magellanic O-type stars, 11 of which being in the LMC, for which ultraviolet STIS spectra were available in the HST Archive and optical spectra were secured with the Boller & Chivens Spectrograph at the Clay 6.5m (Magellan II) telescope at Las Campanas. Four of the LMC sources studied by these authors were included in a reanalysis, where results obtained with FASTWIND (Puls et al. 2005; Rivero González et al. 2011) and CMFGEN (Hillier & Miller 1998) were compared (Massey et al. 2013). Though this constitutes a promising start indeed, the morphological properties among O stars are so complex that still larger samples are required for robust tests of stellar evolution.

\* Based on observations collected at the European Southern Observatory under program ID 182.D-0222.

The Tarantula nebula in the LMC is particularly rich in O-type stars, containing hundreds of these objects. It has a well-constrained distance modulus of 18.5 mag (Pietrzyński et al. 2013) and only a modest foreground extinction, making it an ideal laboratory to study entire populations of massive stars. This motivated the VLT-FLAMES Tarantula Survey (VFTS), a multi-epoch spectroscopic campaign that targeted 360 O-type and approximately 540 later-type stars across the Tarantula region, spanning a field several hundred light years across (Evans et al. 2011, hereafter Paper I).

In the present paper within the VFTS series, we analyze the properties of the 72 presumed single O-type giants, bright giants, and supergiants in the VFTS sample. In all likelihood, not all of them are truly single stars. Establishing the multiplicity properties of the targeted stars was an important component of the VFTS project (Sana et al. 2013; Dunstall et al. 2015) and the observing strategy was tuned to enable the detection of close pairs with periods up to  $\sim 1000$  days, that is, those that are expected to interact during their evolution (e.g., Podsiadlowski et al. 1992). The finite number of epochs resulted in an average detection probability of approximately 70%, implying that some of our targets may be binaries. Additionally, post-interaction systems may be disguised as single stars by showing no or negligible radial velocity variations (de Mink et al. 2014). By confronting the stellar characteristics with evolutionary models for single stars we may not only test these models, but also identify possible post-interaction systems if their properties appear peculiar and contradict basic predictions from single-star models.

The outflows of O III to O I stars are dense and most of them feature signatures of mass-loss in  $H\alpha$  and  $He\ II\ \lambda 4686$ , allowing us to assess their wind strength. The stellar and wind properties of the dwarfs are presented in Sabín-Sanjulián et al. (2014, hereafter Paper XIII) and Sabín-Sanjulián et al. (subm.). Those of the most massive stars in the VFTS sample (the Of and WNh stars) have been presented in Bestenlehner et al. (2014, hereafter Paper XVII). Combining these results with those from this paper enables a confrontation with wind-strength predictions using a sample that is unprecedented in size.

The layout of the paper is as follows. Section 2 describes the selection of our sample. The spectral analysis method is described in Section 3. The results are presented and discussed in Section 4. Finally, a summary is given in Section 5.

## 2. Sample and data preparation

The VFTS project and the data have been described in Paper I. Here we focus on a subset of the O-type star sample that has been observed with the Medusa fibers of the VLT-FLAMES multi-object spectrograph: the presumably single O stars with luminosity class (LC) III to I. The total Medusa sample contains 332 O-type objects observed with the Medusa fiber-fed Giraffe spectrograph. Their spectral classification is available in Walborn et al. (2014). Among that sample, Sana et al. (2013) have identified 116 spectroscopic binary (SB) systems from significant radial velocity (RV) variations with a peak-to-peak amplitude ( $\Delta RV$ ) larger than  $20\text{ km s}^{-1}$ . The remaining 216 objects either show no significant or significant but small RV variations ( $\Delta RV \leq 20\text{ km s}^{-1}$ ). They are presumed single stars although it is expected that up to 25% of them are undetected binaries (see Sana et al. 2013). The rotational properties of the O-type single and binary stars in the VFTS have been presented by Ramírez-Agudelo et al. (2013, hereafter Paper XII) and Ramírez-Agudelo et al. (2015).

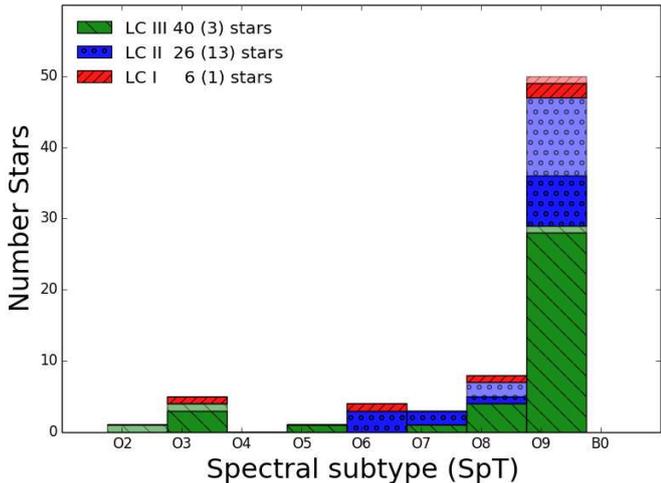


**Fig. 1.** Spectral-type distribution of the O-type stars in our sample, binned per spectral subtype (SpT). Different colors and shadings indicate different luminosity classes (LC); see legend. The legend also gives the total number of stars in each LC class (e.g., 40 LC III). In parentheses we provide the number of stars that were given an ambiguous LC classification within each category in Walborn et al. (2014) (e.g., 3 in LC III). They are plotted in their corresponding category with lower opacity (see main text for details).

Here we focus on the 72 presumably single O stars with LC III to I. The remaining 31 spectroscopically single objects could not be assigned a LC classification (see Walborn et al. 2014) and for that reason are discarded from the present analysis. For completeness, we do however provide their parameters (see Sect. 3.7.2).

Our sample contains 37 LC III, 13 LC II, and 5 LC I objects. In addition to these 55 stars, there are 17 objects with a somewhat ambiguous LC, namely: 1 LC III-IV, 2 LC III-I, 10 LC II-III, 3 LC II-B0 IV, and 1 LC I-II. We adopted the first listed LC classification bringing the total sample to 40 giants, 26 bright giants, and 6 supergiants. Figure 1 displays the distribution of spectral subtypes and shows that 69% of the stars in the sample are O9-O9.7 stars. The lack of O4-5 III to I stars is in agreement with statistical fluctuations due to the sample size. The number of such objects in the full VFTS sample is comparable to that of O3 stars; they are however almost all of LC V or IV (see Fig. 1 in Paper XII and Table 1 in Walborn et al. 2014). There are only a few Of stars and no Wolf Rayet (WR) stars in our sample. These extreme and very massive stars in the VFTS have been studied in Paper XVII (see Sect. 3).

The spatial distribution of our sample is shown in Fig. 2. The stars are concentrated in two associations, NGC 2070 (in the centre of the image), and NGC 2060 (6.7' south-west of NGC 2070), although a sizeable fraction are distributed throughout the field of view. For consistency with other VFTS papers, we refer to stars located further away than 2.4' from the centers of NGC 2070 and NGC 2060 as the stars *outside of star-forming complexes*. These may originate from either NGC 2070 or 2060 but may also have formed in other star-forming events in the 30 Dor region at large. A circle of radius 2.4' (or 37 pc) around NGC 2070 contains 22 stars from our sample: 13 are of LC III, 8 are of LC II and 1 is of LC I. NGC 2060 contains 24 stars in a similar sized region and is believed to be somewhat older (Walborn & Blades 1997). Accordingly, it contains a larger frac-

tion of LC II and I stars (63%; 15 out of 24) than NGC 2070 (40%).

## 2.1. Data preparation

The VFTS data are multi-epoch and multi-setting by nature. To increase the signal-to-noise of individual epochs and to simplify the atmosphere analysis process, we have combined, for each star, the spectra from the various epochs and setups into a single normalized spectrum per object. We provide here a brief overview of the steps taken to reach that goal. We assumed that all stars are single by nature, that is, that no significant RV shift between the various observation epochs needs to be accounted for. This assumption is validated for our sample (see above), which selects either stars with no statistically significant RV variation, or significant but small RV shifts ( $\Delta RV < 20 \text{ km s}^{-1}$ ; hence less than half the resolution element of  $\sim 40 \text{ km s}^{-1}$ ).

For each object and setup, we started from the individual-epoch spectra normalized by Sana et al. (2013) and first rejected the spectra of insufficient quality ( $S/N < 5$ ). Subsequent steps are:

- i. Rebinning to a common wavelength grid, using the largest common wavelength range. Step sizes of  $0.2 \text{ \AA}$  and  $0.05 \text{ \AA}$  are adopted for the LR and HR Medusa-Giraffe settings, respectively.
- ii. Discarding spectra with a  $S/N$  lower by a factor of three, or more, compared to the median  $S/N$  of the set of spectra for the considered object and setup;
- iii. Computing the median spectrum;
- iv. At each pixel, applying a  $5\sigma$ -clipping around the median spectrum, using the individual error of each pixel;
- v. Computing the weighted average spectrum, taking into account the individual pixel uncertainties and excluding the clipped pixels;
- vi. Re-normalizing the resulting spectrum to correct for minor deviations that have become apparent thanks to the improved  $S/N$  of the combined spectrum. The typical normalization error is better than 1% (see Appendix A in Sana et al. 2013). The obtained spectrum is considered as the final spectrum for a given star and a given observing setup.
- vii. The error spectrum is computed through error-propagation throughout the described process.

Once we have combined the individual epochs, we still have to merge the three observing setups. In particular, the averaged LR02 and LR03 spectra of each object are merged using a linear ramp between  $4500$  and  $4525 \text{ \AA}$ . This implies that below  $4500 \text{ \AA}$  the merged spectrum is from LR02 exclusively and that above  $4525 \text{ \AA}$  it is from LR03. In particular, the information on the He II  $\lambda 4541$  line present in LR02 is discarded despite the fact that there are twice as many epochs of LR02 than of LR03. This is mainly due to (i) a sometimes uncertain normalization of the He II  $\lambda 4541$  region in LR02, as the line lies very close to the edge of the LR02 wavelength range, and (ii) the fact that LR02 and LR03 setups yield different spectral resolving power. Hence, we decided against the combination of data that differ in resolving power in such an important line for atmosphere fitting. While we might thus lose in  $S/N$ , we gain in robustness. In the  $4500 - 4525 \text{ \AA}$  transition region, we note that we did not correct for the difference in resolving power between LR02 and LR03. For most objects, no lines are visible there. Finally, HR15N was simply added as there is no overlap.

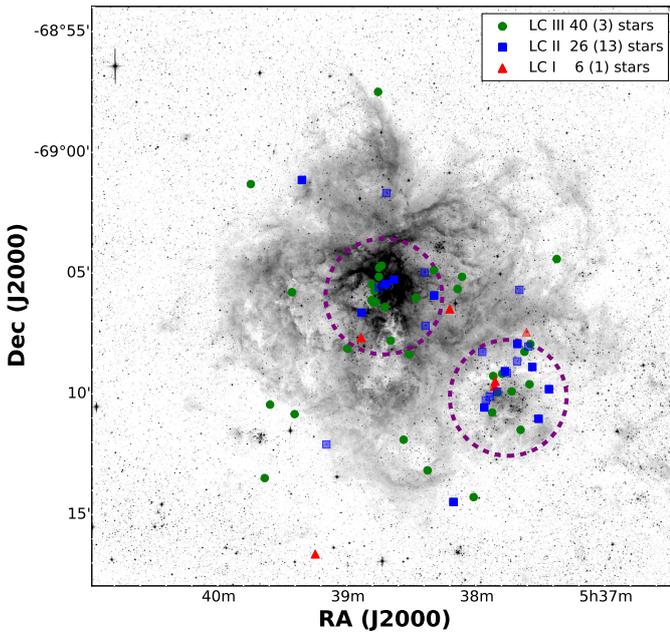


**Fig. 2.** Spatial distribution of the presumably single O-type stars as a function of LC. North is to the top; east is to the left. The circles define regions within  $2.4'$  of NGC 2070 (central circle) and NGC 2060 (south-west circle). Different symbols indicate LC: III (circles), II (squares), I (triangles). Note that because of crowding a considerable fraction of the sources overlap. Lower opacities again denote sources with an ambiguous LC classification, similar as in Fig. 1.

### 3. Analysis method

To investigate the atmospheric properties of our sample stars, we obtained the stellar and wind parameters by fitting synthetic spectra to the observed line profiles. This method is described in the following section.

#### 3.1. Atmosphere fitting

The stellar properties of the stars have been determined using an automated method first developed by Mokieim et al. (2005). This method combines the non-LTE stellar atmosphere code `FASTWIND` (Puls et al. 2005; Rivero González et al. 2011) with the genetic fitting algorithm `PIKAIA` (Charbonneau 1995). It allows for a standardized analysis of the spectra of O-type stars by a thorough exploration of the parameter space in affordable CPU time on a supercomputer (see, Mokieim et al. 2006, 2007a,b; Trammer et al. 2011, 2014).

In the present study, we used `FASTWIND` (version 10.1) with detailed model atoms for hydrogen and helium (described in Puls et al. 2005), and in some cases (see below) also for nitrogen (Rivero González et al. 2012a) and silicon (Trundle et al. 2004) as ‘explicit’ elements. Most of the other elements up to zinc were treated as background elements. In brief, explicit elements are those used as diagnostic tools and treated with high precision by detailed atomic models and by means of a co-moving frame transport for all line transitions. The background elements (i.e., the rest) are only needed for the line-blocking/blanketing calculations, and are treated in a more approximate way, though still solving the complete equations of statistical equilibrium for most of them. In particular, parametrized ionization cross sections following Seaton (1958) are used, and a co-moving frame transfer

is applied only for the strongest lines, whilst the weaker ones are calculated by means of the Sobolev approximation. For the abundances of these background elements we adopt solar values by Asplund et al. (2005) scaled down by 0.3 dex to mimic the metal deficiency of the LMC (e.g., Rolleston et al. 2002). The abundance of carbon is further adjusted by  $-1.1$  dex (i.e.,  $[C] = 7.0$ , where  $[X] = \log(X/H)+12$ ) and nitrogen by  $+0.35$  dex (i.e.,  $[N] = 7.7$ ), characteristic for the surfacing of CN- and CNO-cycle products (Brott et al. 2011).

The `PIKAIA` algorithm was used to evolve a population of 79 randomly drawn initial solutions (i.e., a population consisting of 79 individuals) over 300 generations. The population of each subsequent generation was based on selection pressure (i.e., highest fitness) and random mutation of parameters. Convergence was generally achieved after 30-50 generations, depending on the gravity, with lower-gravity objects requiring more generations to reach convergence. Computing a large number of generations beyond the convergence point allows us to fully explore the shape of the  $\chi^2$  minimum while further ensuring that the absolute optimum has been identified. The population survival was based on the *fitness* ( $F$ ) of the models, computed as:

$$F = \left( \frac{\sum_l w_l \cdot \chi_{l,\text{red}}^2}{N_l} \right)^{-1}, \quad (1)$$

where  $\chi_{l,\text{red}}^2$  is the reduced  $\chi^2$  between the data and the model for line  $l$ ,  $w_l$  is a weighting factor, and where the summation is carried out on the number of fitted lines  $N_l$ . We adopt unity for all weights, except for He II  $\lambda 4200$  ( $w = 0.5$ ) and the singlet transition He I  $\lambda 4387$  ( $w = 0.25$ ), for reasons discussed in Mokieim et al. (2005).

While the exploration of the parameter space is based on the fitness to avoid a single line outweighing the others, the fit statistics – and the error bars – are however computed using the  $\chi^2$  statistic, computed in the usual way.

$$\chi^2 = \sum_l \chi_l^2. \quad (2)$$

The algorithm makes use of the normalized spectra to derive the effective temperature ( $T_{\text{eff}}$ ), the surface gravity ( $\log g$ ), the mass-loss rate ( $\dot{M}$ ), the exponent of the  $\beta$ -type wind-velocity law ( $\beta$ ), the helium over hydrogen number density (later converted to surface helium abundance in mass fraction,  $Y$ , through the paper), the microturbulent velocity ( $v_{\text{turb}}$ ) and the projected rotational velocity ( $v_e \sin i$ ). For additional notes on  $v_e \sin i$ , we refer the reader to Sect. 3.7.1.

While the method, in principle, allows for the terminal wind velocity ( $v_\infty$ ) to be a free parameter, this quantity cannot be constrained from the optical diagnostic lines. Instead, we adopted the empirical scaling of  $v_\infty$  with the escape velocity ( $v_{\text{esc}}$ ) of Kudritzki & Puls (2000), taking into account the metallicity ( $Z$ ) dependence of Leitherer et al. (1992):  $v_\infty = 2.65 v_{\text{esc}} Z^{0.13}$ . In doing so, we corrected the Newtonian gravity as given by the spectroscopic mass for radiation pressure due to electron scattering. In units of the Newtonian gravity, this correction factor is  $(1 - \Gamma_e)$ , where  $\Gamma_e$  is the Eddington factor for Thomson scattering. This treatment of terminal velocity ignores the large scatter that exists around the  $v_\infty$  versus  $v_{\text{esc}}$  relation (see discussions in Kudritzki & Puls 2000; Garcia et al. 2014). However, consistency checks performed in Sect. 3.4.3 indicate that this is not a major issue.

For each star in our sample, up to 12 diagnostic lines are adjusted: He I+II  $\lambda 4026$ , He I  $\lambda 4387$ , 4471, 4713, 4922, He II  $\lambda 4200$ ,

4541, 4686, H $\delta$ , H $\gamma$ , H $\beta$ , and H $\alpha$ . For a subset of stars (those with the earliest spectral subtypes, and mid- and late-O supergiants), our set of H and He diagnostic lines was not sufficient to accurately constrain their parameters. In these cases, we also adjusted nitrogen lines in the spectra and considered the nitrogen surface abundance to be a free parameter. Specifically, we included the following lines in the list of diagnostic lines used: N II  $\lambda$ 3995, N III  $\lambda$ 4097, 4103, 4195, 4200, 4379, 4511, 4515, 4518, 4523, 4634, 4640, 4641, N IV  $\lambda$ 4058 and N V  $\lambda$ 4603, 4619. Tables C.1-C.3 summarize, for each star, the diagnostic lines that have simultaneously been considered in the fit. The fitting results for each object were visually inspected. Residuals of nebular correction were manually clipped, after which the fitting procedure was repeated. The best-fit model and the set of acceptable models, for every star, are displayed in Appendix E (see also Sect. 3.2).

The de-reddened absolute magnitude and the RV of the star are needed as input parameters; the first is used to determine the object luminosity and hence the radius, while the second is used to shift the model and data to the same reference frame. While both Mokiem et al. (2005, 2006, 2007a) and Tramper et al. (2011, 2014) used the V-band magnitude as a photometric anchor, we choose to use the K-band magnitude ( $M_K$ ) to minimise the impact of uncertainties on the individual reddening of the objects in our sample. We determined  $M_K$  using the VISTA observed K-band magnitude (Rubele et al. 2012), adopting a distance modulus to the Tarantula nebula of 18.5 mag (see Paper I) and an average K-band extinction ( $A_K$ ) of 0.21 mag (Maíz-Apellániz et al., in prep.). The obtained  $M_K$  values are provided in Table C.4 and C.5, for completeness. As for the RV values we used the measurements listed in Sana et al. (2013).

### 3.2. Error calculation

The parameter fitting uncertainties were estimated in the following way. For each star and each model, we calculated the probability ( $P$ ) that the  $\chi^2$  value as large as the one that we observed is not a result of statistical fluctuation:  $P = 1 - \Gamma(\chi^2/2, \nu/2)$ , where  $\Gamma$  is the incomplete gamma function and  $\nu$  the number of degrees of freedom.

Because  $P$  is very sensitive to the  $\chi^2$  value, we re-normalized all  $\chi^2$  values such that the best fitting model of a given star has a reduced  $\chi^2$  ( $\chi_{\text{red}}^2$ ) equal to unity. We thus implicitly assumed that the model with the smallest  $\chi^2$  represents the data and that deviations of the best model's  $\chi_{\text{red}}^2$  from unity result from under- or overestimated error bars on the normalized flux. This approach is valid if the best-fit model represents the data, which was visually checked for each star (see Sect. 3.7 and Appendix E). Finally, the 95% confidence intervals on the fitted parameters were obtained by considering the range of models that satisfy  $P(\chi^2, \nu) > 0.05$ . The latter can approximately be considered as  $\pm 2\sigma$  error estimates in cases where the probability distributions follow a Gaussian distribution.

The finite exploration of parameter space may however result in an underestimate of the confidence interval in the case of poor sampling near the borders  $P(\chi^2, \nu) = 0.05$ . As a first attempt to mitigate this situation, we adopt as boundaries of the 95% confidence interval the first models that do not satisfy  $P(\chi^2, \nu) = 0.05$ , hence making sure that the quoted confidence intervals are either identical or slightly larger than their exact 95% counterparts. However, for approximately 10% of the boundaries so determined, the results were still leading to unsatisfactory small, or large, upper and lower errors. We then turned to fitting the  $\chi^2$

distribution envelopes. The left- and right-hand part of the envelopes were fitted separately for all quantities using either a 3rd- or 4th degree polynomial or a Gaussian profile. The intersects of the fitted envelope with the critical  $\chi^2$  threshold defined above ( $P(\chi^2, \nu) = 0.05$ ) for the function that best represented the envelope were then adopted as upper- and lower-limit for the 95%-confidence intervals.

The obtained boundaries of the confidence intervals, relative to the best-fit value, are provided in Table C.4. For some quantities and for some stars, these boundaries are relatively asymmetric with respect to the best-fit values. Hence, the total range covered by the 95% confidence intervals needs to be considered to understand the typical error budget in our sample stars, that is, not only the lower- or upper-boundaries. In Fig. 3, we show the distribution of these widths for all model parameters that have their confidence interval constrained (i.e., excluding upper/lower limits). The median values of these uncertainties are 2090 K for  $T_{\text{eff}}$ , 0.25 dex for  $\log g$ , and 0.11 for  $Y$ . For those sources that have their mass-loss rates constrained, the median uncertainty in  $\log \dot{M}$  is 0.3 dex. For the projected spin velocities it is 44 km s $^{-1}$ . We note that for some sources, the formal error estimates are very small. This is particularly so in cases where nitrogen lines are used as diagnostics, which tend to place stringent limits on the effective temperature, hence indirectly on the surface gravity, and the mass-loss rate. Results related to sources for which nitrogen was included in the analysis have been given a different color in Fig. 3.

### 3.3. Sources of systematic errors

It is important to stress that the confidence intervals given in Table C.4 represent the validity of the models as well as the formal errors of the fits, that is, uncertainties measuring statistical variability. They do not account for systematic uncertainties, which may be significant. Here we discuss possible sources of this type of uncertainty that may impact the accuracy of our results.

Systematic errors may relate to model assumptions, continuum placement biases, the assumed distance to the LMC, or an uncertain extinction, for example. Regarding the adopted model atmosphere, Massey et al. (2013) performed a by-eye analysis of ten LMC O-type stars using both CMFGEN (Hillier & Miller 1998) and FASTWIND. They report a systematic difference in the derived gravity of 0.12 dex, with CMFGEN values being higher. They argue that differences in the treatment of the electron scattering wings might explain the bulk of this difference, a treatment that is more refined in CMFGEN. A systematic error in the normalization of the local continuum may also impact the gravity estimate. If by-eye judgement would place it too high by 1% (where the typical normalization error is better than 1%; see Sect. 2.1) for all relevant diagnostic lines, this would lead to a gravity that is higher by less than 0.1 dex. We do not, however, anticipate such a large systematic normalization error. The distance to the LMC is accurate to within 2% (Pietrzyński et al. 2013). We adopt a mean K-band extinction of 0.21 mag (see Sect. 3.1). Typical deviations of this mean value are not larger than 0.1 mag (Maíz-Apellániz et al. in prep.), hence correspond to an uncertainty in the luminosity of less than 10%.

Other systematic uncertainties may be present; for instance model assumptions that impact both a FASTWIND and CMFGEN analysis. Examples are the neglect of macro-turbulence or the assumption of a spherical and constant mass-loss rate outflow.

Systematic (quantifiable and non-quantifiable) errors will impact the formal confidence intervals discussed in Sect. 3.2. In

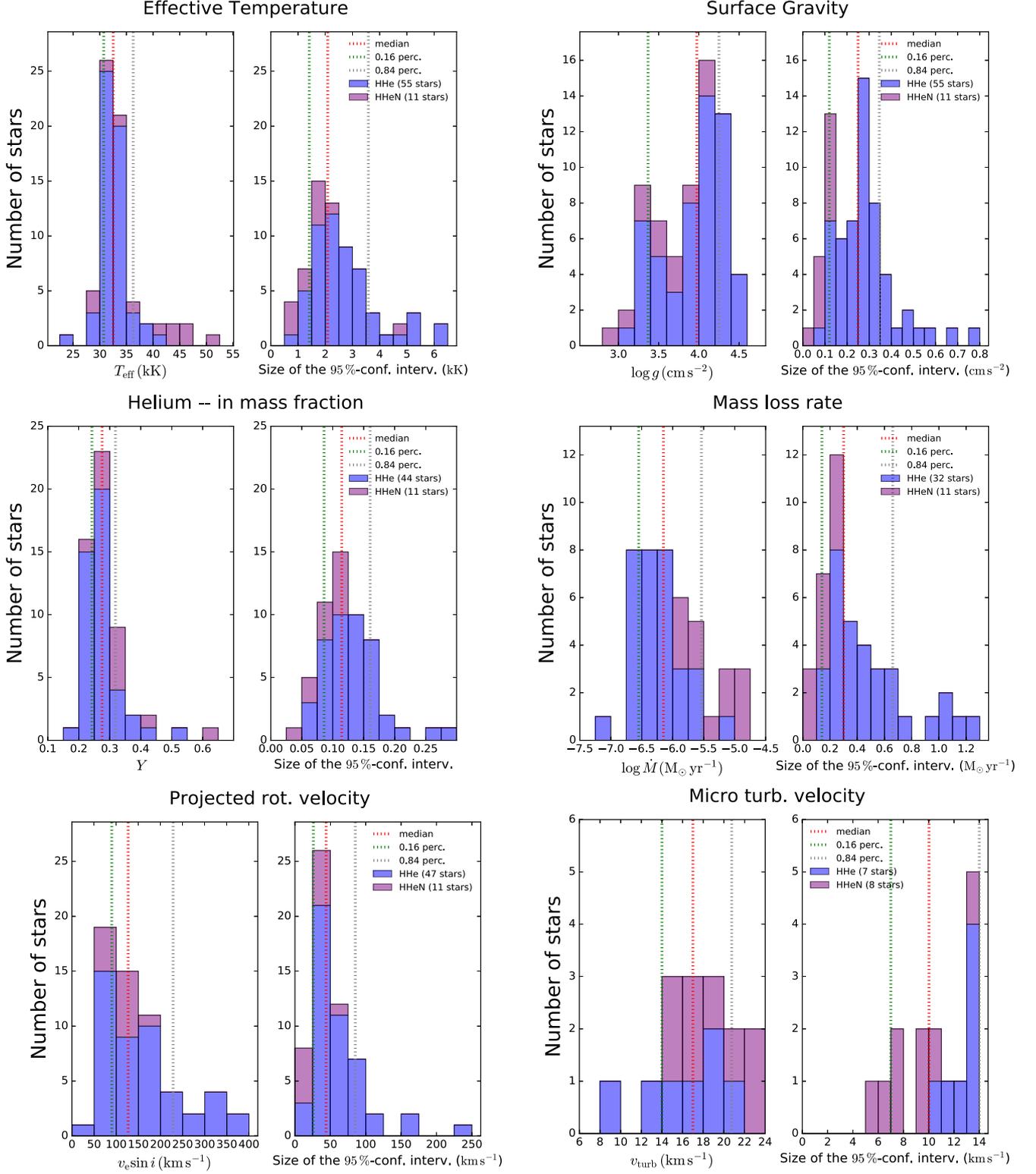


**Fig. 3.** Range of each fitted parameter (left panels of each set) and accompanying range of 95% confidence interval (right panel of each set) in the same unit. Colors have been used to differentiate between stars that have been analyzed using hydrogen and helium lines (HHe) and those for which also nitrogen lines (HHeN) were considered (see also Sect. 3.1). The distributions exclude stars for which only upper/lower limits could be determined, hence the number of stars shown in a panel depends on the parameter that is investigated. In each panel, the median value and the 16th and 84th percentiles are shown using vertical lines.

those cases where the quoted confidence intervals are approximately equal to their respective medians or larger, the systematic errors will likely contribute modestly to the total uncertainties.

In cases where the formal errors are small, we caution the reader that systematic uncertainties may be larger than the statistical uncertainties presented in Table C.4.



noted these six objects as having a somewhat problematic spectral classification. Interestingly, our fits of these six stars often implied a helium abundance significantly lower than the primordial value, which may be the result of line dilution by the continuum of the companion. We decided to discard these stars from our discussion, opting for a sample of  $72 - 6 = 66$  high-quality fits only and minimizing the risk of misinterpretations. We do provide the obtained parameters and formal uncertainties of these six stars in Table C.4 but warn against possible systematic biases.

All other spectral fits were screened by eye to assess their quality. We concluded that all fits were acceptable within the range of models that pass our statistical criteria except those of six objects without LC (VFTS 145, 360, 400, 446, 451, and 565). We also provide the obtained parameters of these six stars in Table C.5 but warn that they may not be representative of the stars physical parameters as their fits have limited quality.

### 3.7. Limitations of the method

We discuss two limitations of the method in more detail, that is, the neglect of macro-turbulence and the lack of a diagnostics that allows us to constrain the spatial velocity gradient of the outflow.

#### 3.7.1. Extra line-broadening due to macro-turbulent motions

When comparing the models with the data, we take into account several sources of spectral line broadening: intrinsic broadening, rotational broadening, and broadening due to the instrumental profile. However, we do not take into account the possibility of extra-broadening as a result of macro-turbulent motions in the stellar photosphere (e.g., Gray 1976). This approach is somewhat different to that of Paper XII, in which a Fourier transform method was used to help differentiate between rotation and macro-turbulent broadening, neglecting intrinsic line broadening and given a model for the behavior of macro-turbulence (we refer to Paper XII for a discussion).

Appendix A compares the rotation rates of the sample of 66 stars obtained through both methods. The systematic difference ( $\Delta v_e \sin i$  [this study - Paper XII]) is approximately  $7 \text{ km s}^{-1}$  with a standard deviation of approximately  $21 \text{ km s}^{-1}$ . This is within the uncertainties discussed in Paper XII. At projected spin velocities below  $160 \text{ km s}^{-1}$  the present measurements may overestimate  $v_e \sin i$  by up to several tens of  $\text{km s}^{-1}$  in cases where macro-turbulence is prominent. Though, the best of our knowledge, there are no theoretical assessments of the impact of macro-turbulence on the determination of the stellar parameters, we do not expect the differences in  $v_e \sin i$  to affect the determination of other stellar properties in any significant way as the  $v_e \sin i$  measurements of both methods are within uncertainties.

#### 3.7.2. Wind-velocity law

The spatial velocity gradient, measured by the exponent  $\beta$  of the wind-velocity law becomes unconstrained if the diagnostic lines which are sensitive to mass-loss rate ( $\text{H}\alpha$  and  $\text{He II } \lambda 4686$ ) are formed close to the photosphere. In such cases, the flow velocity is indeed still low compared to  $v_\infty$ . In an initial determination of the parameters, we let  $\beta$  be a free parameter in the interval [0.8, 2.0]. In approximately half of the cases, the fit returned a central value for  $\beta$  larger than 1.2 and with large uncertainties. From theoretical computations, such a large acceleration parameter is not expected for normal O stars and we identified these sources

as having an unconstrained  $\beta$ . Given the large percentage of stars that fell in this category and the potential impact of  $\beta$  on the derived mass-loss rate, we decided to adopt  $\beta = 0.9$  for giants and 0.95 for bright giants and supergiants, following theoretical predictions by Muijres et al. (2012). For the 31 O stars that could not be assigned a LC, we adopted the canonical value  $\beta = 1$  (see Table C.5). We will discuss the impact of this assumption in Sect. 4.5.

## 4. Results and discussion

We discuss our findings for the effective temperature, gravity, helium abundance, mass loss, and mass, and place these results in the broader context of stellar evolution, mass-loss behavior, and mass discrepancy.

### 4.1. Effective temperature vs. spectral subtype calibrations

Figure 4 plots the derived effective temperature for 53 giants, bright giants and supergiants as a function of spectral subtype. This sample of 53 stars corresponds to the high-quality fits (66 stars) minus the stars that have a somewhat ambiguous luminosity classification (17 minus the newly confirmed binaries VFTS 093, 171, 332, and 333 fits, hence 13 stars; we refer to Sects. 2 and 3.6). For LC III and LC II stars, the scatter at late spectral type is too large to be solely explained by measurement errors and may thus also reflect intrinsic differences in gravity, hence in evolutionary state (for a discussion, see Simón-Díaz et al. 2014). Added to the figure are results for 18 LC III to I LMC stars by Mokiem et al. (2007b). These were analyzed using the same fitting technique, save that these authors did not use nitrogen lines in cases where either  $\text{He I}$  or  $\text{He II}$  lines were absent (see Sect. 3.1). Both our sample and that of Mokiem et al. yield results that are compatible with each other, therefore we combine both samples in the remainder of this section.

Though the overall trend in Fig. 4 is clearly that of a monotonically decreasing temperature with spectral subtype, such a trend need not necessarily reflect a linear relationship. Work by Rivero González et al. (2012a,b) for early-O dwarfs in the LMC, for instance, suggests a steeper slope at the earliest subtypes (O2-O3). This seems to be supported by first estimates of the properties of O2 dwarfs in the VFTS by Sabin-Sanjulián et al. (2014). The presence of such an upturn starting at spectral subtype O4 is not confirmed in Fig. 4. The three O2 III stars (all from Mokiem et al.) do show a spread that may be compatible with a steeper slope for giants but such an increased slope is not yet needed at subtype O3. Furthermore, the only two O2 I and O3 I stars in Fig. 4 are perfectly compatible with a constant slope down to the earliest spectral sub-types for the supergiants. In regards to the insufficient number of stars, to fully test for the presence of an upturn at subtype O2, we limit our  $T_{\text{eff}}$ -SpT calibrations to subtypes O3 and later.

A shallowing of the  $T_{\text{eff}}$ -SpT relation at subtypes later than O9 (relative to the O3-O9 regime) is also relatively conspicuous in Fig. 4. We too exclude this regime from the relations given below, also because the luminosity classification of this group in particular may be debated (see Sect. 4.2). We thus aim to derive  $T_{\text{eff}}$ -SpT relations for LMC O-type stars in the regime O3-O9. To do so, we used a weighted least-square linear fit to adjust the relation

$$T_{\text{eff}} = a + b \times \text{SpT}, \quad (3)$$

where the spectral subtype is represented by a real number, for example,  $\text{SpT} = 6.5$  for an O6.5 star. Figure 5 shows these linear

fits for our sample and that of Mokieim et al. (2007a) combined, for each luminosity class separately. The fit coefficients and their uncertainties are provided in Table 1.

A comparison of our combined LC III, II and I relations with theoretical results for a LMC metallicity is not feasible as, to our knowledge, such predictions are not yet available. One may anticipate that a LMC calibration would be shifted up to higher temperatures, as, in a lower metallicity environment, the effects of line blocking/blanketing are less important than in a high-metallicity environment. Thus, fewer photons are scattered back, contributing less to the mean intensity in those regions where the He I lines are formed. Consequently, a higher  $T_{\text{eff}}$  is needed to reach the same degree of ionization for stars in the LMC compared to those with a higher metal abundance (which have stronger blocking/blanketing, see Repolust et al. 2004). In Fig. 5, we compare our results to the LC III and I empirical calibrations of Martins et al. (2005, their equation 2) for Galactic stars. Below we discuss the results for LC III, II, and I separately:

- *Giants (LC III)*: The slope of the  $T_{\text{eff}}$ -SpT relation for giants is in excellent agreement with the (observational) Martins et al. (2005) calibration, though an upward shift of approximately 1 kK is required to account for the lower metallicity. Doran et al. (2013) report that a +1 kK shift is required to match the LMC dwarfs, but that no shift seems required for O-giants. Our results suggest that this upward shift should be applied to this category as well.
- *Bright giants (LC II)*: The  $T_{\text{eff}}$ -SpT relation for the bright giants is relatively steep, and crosses the relations for the giants and supergiants. As explained in the notes for individual stars (Appendix D), the spectra of some of these stars are peculiar. We also note that in the Hertzsprung-Russell diagram the O II stars do not appear to constitute a distinct group intermediate between the giants and supergiants (see Figs. 6 and 9); rather, they mingle between the O V and I stars. This might explain their behavior in Fig. 5 and implies that one should be cautious in using this relation as a calibration. We recommend to refrain from doing so and to wait until more data become available.
- *Supergiants (LC I)*: Our supergiant sample is smaller than that of the giants and some O I stars have peculiar spectra (Appendix D), yet it is the largest LMC supergiants sample assembled so far and hence worthy of some in-depth discussion. As also observed at Galactic metallicity (Martins et al. 2005), our derived  $T_{\text{eff}}$ -SpT relation for supergiants is shallower than that for giants. The slope for the supergiants is even more shallow at LMC than obtained by Martins et al. in the Milky Way. Furthermore, the upward shift measured for LMC V and III stars compared to those in the Galaxy is not seen for the supergiants. If anything, a downward shift is present at the earliest spectral types. Within uncertainties however, one may still accept the Galactic-metallicity relation derived for LC I by Martins et al. as a reasonable representation of the LMC supergiants. A larger sample would be desirable to confirm or discard these preliminary conclusions as well as to investigate the physical origin of the different metallicity effects for LC I objects compared to LC V and III stars.

#### 4.2. Gravities and luminosity classification

We present the Newtonian gravities graphically using the  $\log g_c - \log T_{\text{eff}}$  diagram and the spectroscopic Hertzsprung-Russell (sHR) diagram (Fig. 6). In doing so, the gravities were

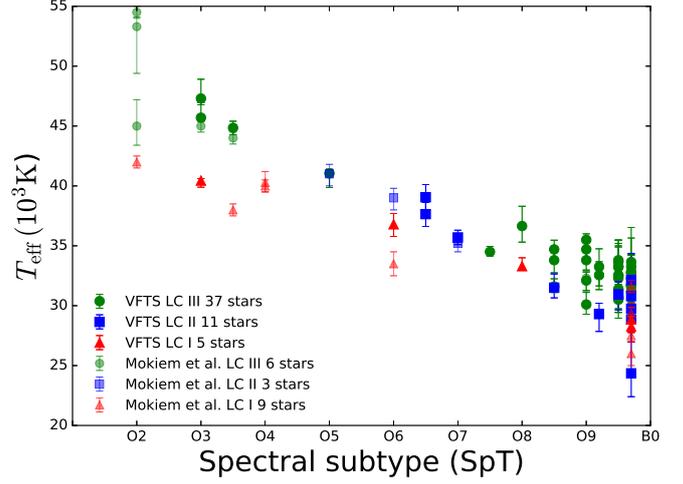


**Fig. 4.** Effective temperature vs. spectral subtype for the O-type with well defined LC (see main text). The lower-opacity symbols give the results for the sample of LMC stars investigated by Mokieim et al. (2007b).

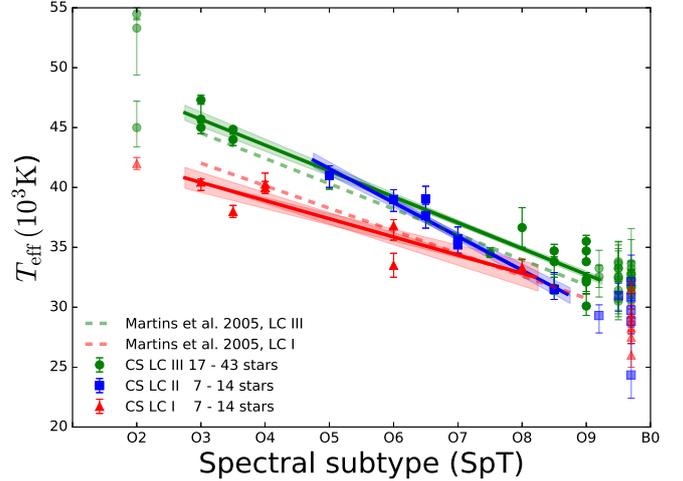


**Fig. 5.** Effective temperature vs. spectral subtype but now displaying fits that combine our sample with that of Mokieim et al. (2007b): CS = Combined sample (see main text). Stars with spectral subtype O2-3 or later than O9 have been plotted with lower opacity. The dashed lines give the theoretical calibrations of Martins et al. (2005) for Galactic class III and I stars. The leading number in the legend refers to the total number of O3-O9 stars for which the fit has been derived. The trailing number refers to the total number of stars in each sample.

corrected for centrifugal acceleration using  $\log g_c = \log [g + (v_e \sin i)^2 / R]$  (see also Herrero et al. 1992; Repolust et al. 2004). The sHR diagram shows  $\mathcal{L}$  versus  $T_{\text{eff}}$ .  $\mathcal{L} \equiv T_{\text{eff}}^4 / g_c$  is proportional to  $L/M$ , thus to  $\Gamma_e / \kappa$ , where  $\kappa$  is the flux-mean opacity (see Langer & Kudritzki 2014). For a fixed  $\kappa$ , the vertical axis of this diagram thus sorts the stars according to their proximity to the Eddington limit: the higher up in the diagram the closer their atmospheres are to zero effective gravity (see also Castro et al. 2014).

Figure 6 shows both diagrams for our stars. We have supplemented them with VFTS LC V stars analyzed in Paper XIII. Stars that evolve away from the ZAMS increase their radii, and

**Table 1.**  $T_{\text{eff}}$ -SpT linear-fit parameters and their  $1\sigma$  error bars derived for stars with spectral subtypes O3 to O9 in the combined sample (see text).

Sample	# stars	$a$ (kK)	$b$ (kK)
LC III	17	$52.17 \pm 1.03$	$-2.15 \pm 0.14$
LC II	7	$55.71 \pm 2.07$	$-2.83 \pm 0.31$
LC I	7	$44.97 \pm 1.87$	$-1.52 \pm 0.36$

hence decrease their surface gravity. Therefore, it is expected that the different luminosity classes are separated in these diagrams, that is, stars assigned a lower roman numeral are located further from the ZAMS. This behavior is clearly visible for the supergiants that seem to be the most evolved stars along the main sequence. The bright giants mingle with the supergiants, though some, at 25–30  $M_{\odot}$  reside where the dwarf stars dominate. They do not appear to form a well defined regime intermediate between giants and supergiants, though it should be mentioned that the sample size of these stars is small.

At initial masses of approximately 60  $M_{\odot}$  and higher, giants and bright giants appear closer to the ZAMS. This is the result of a relatively high mass-loss rate, as the morphology of He II  $\lambda 4686$  – the main diagnostic used to assign luminosity class – traces wind density. At initial masses in-between approximately 18  $M_{\odot}$  and 60  $M_{\odot}$ , the dwarf phase clearly precedes the giant and bright giant phase. However, at lower initial masses the picture is more complicated. Here a group of late-O III and II stars populate the regime relatively close to the ZAMS, where dwarf stars are expected. The properties of these stars are indeed more characteristic for LC V objects; they have gravities  $\log g_c$  between 4.0 and 4.5 and radii of approximately 5–8  $R_{\odot}$ . Consequently, their absolute visual magnitudes are fainter than calibrations suggest (Walborn 1973). In addition, these objects display higher spectroscopic masses than evolutionary masses (see Sect. 4.6 and Fig. 12).

What could explain this peculiar group of stars? Though we do not want to exclude the possibility that these objects belong to a separate physical group, we do find that they populate a part of the HRD where few dwarf O stars are actually seen (see Sect. 4.4). A simple explanation may thus be an intricacy with the LC classification.

The spectral classification in the VFTS is described in Walborn et al. (2014). For the late-O stars, following, for example Sota et al. (2011), it relies on the equivalent width ratio He II  $\lambda 4686$  / He I  $\lambda 4713$  as its primary luminosity criterion. The relative strength of Si IV to He I absorption lines may serve as a secondary criteria, a measure that is somewhat susceptible to metallicity effects (see Walborn et al. 2014). The Si IV / He I ratio is however the primary classifier in early-B stars.

Though He II  $\lambda 4686$  / He I  $\lambda 4713$  is the primary criterion in the VFTS, the group of problematic stars being discussed here have Si IV weaker than expected for LC III, favoring a dwarf or sub-giant classification. Indeed, it is often for this reason that the classification of these stars is lower rated in Walborn et al. (2014). Other reasons for the problematic classification of these stars may be relatively poor quality spectra and an inconspicuous binary nature. Regarding the latter possibility, we mention that a similar behavior is seen in some Galactic O stars, as discussed in Sota et al. (2014) and in the third paper of the Galactic O-Star Spectroscopic Survey series (Maíz Apellániz et al. 2016). More specifically, it is seen in the A component of  $\sigma$  Ori AB, that this star itself is a spectroscopic binary. For this system, Simón-Díaz et al. (2011, 2015) find that the spectrum is the composite of that

**Table 2.** Frequency of stars from different sub-samples that display a helium abundance by mass ( $Y$ ) larger than the specified limit by at least  $2\sigma_Y$ . The sample consists of 66 sources. We provide the number of stars with ambiguous LC in parentheses. The error bars indicate the 68%-confidence intervals on the given fractions and were computed using simulated samples and binomial statistics.

Sample	$f(Y)$		
	$> 0.30$	$> 0.35$	$> 0.40$
LC III 39 (2) stars	$0.08 \pm 0.04$	$0.05 \pm 0.04$	$0.00 \pm n/a$
LC II 21 (10) stars	$0.05 \pm 0.05$	$0.00 \pm n/a$	$0.00 \pm n/a$
LC I 6 (1) stars	$0.17 \pm 0.15$	$0.17 \pm 0.15$	$0.17 \pm 0.15$
LC III to I 66 (13) stars	$0.08 \pm 0.03$	$0.05 \pm 0.03$	$0.02 \pm 0.02$

of an O9.5 V and B0.5 V star. Further RV monitoring has indeed revealed that some of these late-O III and II stars are genuine spectroscopic binaries (see annotations in Appendix D).

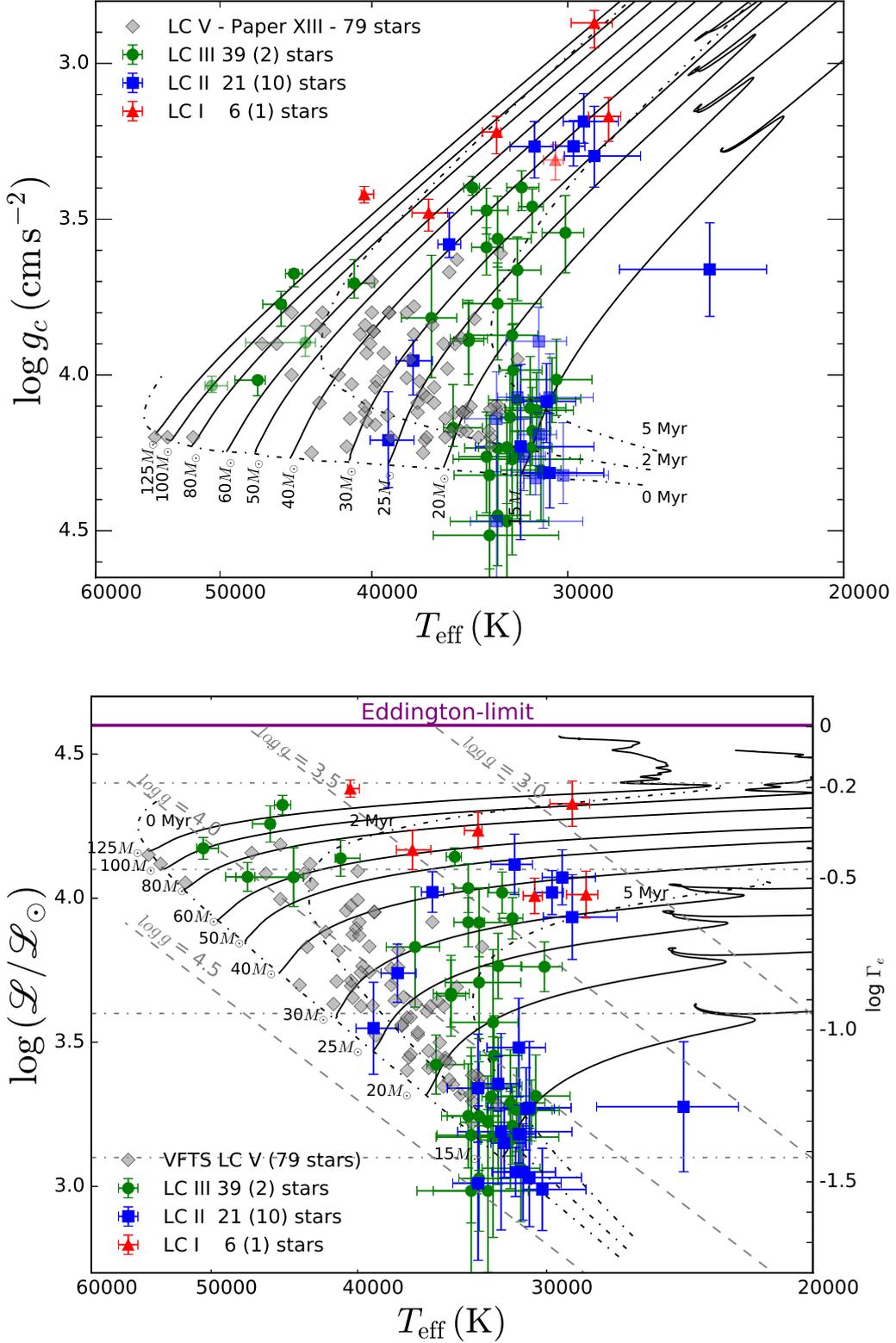
### 4.3. Helium abundance

Figure 7 shows the helium mass fraction  $Y$  as a function of  $v_e \sin i$  (top panel) and  $\log g_c$  (bottom panel). Most of the stars in our sample agree within their 95% confidence intervals with the initial composition of the LMC,  $Y = 0.255 \pm 0.003$ , which has been derived by scaling the primordial value (Peimbert et al. 2007) linearly with metallicity (Brott et al. 2011).

Table 2 summarizes the frequency of stars in the total sample and in given sub-populations that have  $Y$  larger, by at least  $2\sigma_Y$ , than a specified limit. We find that 92.4% of our 66-star sample does not show a clear signature of enrichment given the uncertainties, that is, has  $Y - 2\sigma_Y \leq 0.30$ . Five stars (VFTS 046, 180, 518, 546, and 819), hence 7.6% of our sample, meet the requirement of  $Y - 2\sigma_Y > 0.30$  for a clear signature of enrichment. Interestingly, all these sources have a projected spin velocity less than 200  $\text{km s}^{-1}$  (see upper panel Fig. 7). The lower panel of Fig. 7 plots helium abundance as a function of surface gravity. All sources with  $Y - 2\sigma_Y > 0.35$  have gravities less than or equal to 3.83 dex, though not all sources that have such low gravities have  $Y - 2\sigma_Y > 0.35$ . This conclusion does not change if we take  $\log g_c$  instead.

We ran Monte-Carlo simulations to estimate the number of spuriously detected He-rich stars in our sample, that is, the number of stars that have normal He-abundance but for which the high  $Y$  value obtained may purely result from statistical fluctuations in the measurement process. Given our sample size and measurement errors, we obtained a median number of two spurious detections. Within a 90% confidence interval, this number varies between zero and three. While some detections of He-rich stars in our sample may thus result from statistical fluctuations, it is unlikely that all detections are spurious.

Further, some of the stars appear to have a sub-primordial helium abundance. This is thought to be unphysical, possibly indicating an issue with the analysis such as continuum dilution. Continuum dilution may be caused by multiplicity (either through physical companions or additional members of an unresolved stellar association) and nebular continuum emission, contributing extra flux in the Medusa fiber. In the former case, the extra continuum flux of the companion may weaken the lines, essentially mimicking an unrealistically low helium content. Alternative explanations may be linked to effects of magnetic fields and of (non-radial) pulsations, though, at the present



**Fig. 6.**  $\log g_c$  vs.  $\log T_{\text{eff}}$  (upper panel) and spectroscopic Hertzsprung-Russell (lower panel) diagrams of the O-type giants, bright giants, and supergiants, where  $L \equiv T_{\text{eff}}^4/g_c$  (see Sect. 4.2). Symbols and colors have the same meaning as in Fig. 5. Evolutionary tracks and isochrones are for models that have an initial rotational velocity of approximately  $200 \text{ km s}^{-1}$  (Brott et al. 2011; Köhler et al. 2015). In the lower panel, the right-hand axis gives the classical Eddington factor  $\Gamma_e$  for the opacity of free electrons in a fully ionized plasma with solar helium abundance (c.f. Langer & Kudritzki 2014). The horizontal line at  $\log(L/L_{\odot}) = 4.6$  indicates the location of the corresponding Eddington limit. The dashed straight lines are lines of constant  $\log g$  as indicated. Lower opacities of the green and blue symbols and the numbers in parentheses in the legend have the same meaning as in Fig. 1. [Color version available online].

time, little is known about the impact of these processes on the (apparent) surface helium abundance.

#### 4.3.1. The dependence of $Y$ on the mass-loss rate and rotation rate

As a relatively low surface gravity ( $\log g_c \leq 3.83$ ) seems a prerequisite for surface helium enrichment, envelope stripping through stellar winds may be responsible for the high  $Y$ . To investigate this possibility we plot  $Y$  versus the mass-loss rate relative to the mass of the star ( $\dot{M}/M$ ) in Fig. 8. Here, we adopt  $M_{\text{spec}}$  as a proxy for the mass; using the evolutionary mass  $M_{\text{evol}}$  yields similar results. The quantity  $\dot{M}/M_{\text{spec}}$  is the reciprocal of the momentary stellar evaporation timescale. Also plotted are the set of 26 very massive O, Of, Of/WN, and WNh stars (VMS) analyzed in Paper XVII. At  $\log(\dot{M}/M) \gtrsim -7$ , these stars display a clear correlation with helium abundance. This led Bestenlehner et al. (2014) to hypothesize that, in this regime, mass loss is exposing helium enriched layers.

To explore this further, we compare the data with the main-sequence predictions for  $Y$  versus  $\dot{M}/M$  by Brott et al. (2011) and Köhler et al. (2015) for massive stars in the range of 30–150  $M_{\odot}$ . So far, this is the only set of tracks at LMC metallicity that includes rotation and that covers a wide range of initial spin rates. The plotted tracks have been truncated at 30 kK, that is, approximately where the stars evolve into B-type (super)giants and thus leave our observational sample.

The empirical mass-loss rates used to construct this diagram (i.e., the data points) assume a homogeneous outflow. In Sect. 4.5 we discuss wind clumping, there we point out that for the stars studied here our optical wind diagnostics can be reconciled with wind-strength predictions as used in the evolutionary calculations if the empirical  $\log \dot{M}$  values are reduced by  $\sim 0.4$  dex. Hence, in Fig. 8, the empirical measurements of  $\log(\dot{M}/M)$  should also be reduced by this amount. Regarding the  $\log(\dot{M}/M)$  measurements of Paper XVII (the red squares in Fig. 8), these should also be shifted to lower values. Yet, as the mass estimates obtained in Paper XVII were upper limits and not actual measurements, the reduction in  $\log(\dot{M}/M)$  of these stars may be limited to  $\sim 0.2$ – $0.4$  dex assuming similar clumping properties in Of, Of/WN and WNh stars as applied for O stars.

The upper panel in Fig. 8 shows tracks for initial spin velocities close to 200  $\text{km s}^{-1}$ . Within the framework of the current models, no significant enrichment is expected in the O or WNh phase, with the possible exception of stars initially more massive than  $\sim 150 M_{\odot}$ . We add that mass-loss prescriptions adopted in the evolutionary tracks discussed here account for a bi-stability jump at spectral type B1.5, where the mass-loss rate is predicted to strongly increase (Vink et al. 1999). Beyond the bi-stability jump stars initially more massive than  $\sim 60$ – $80 M_{\odot}$  do show strong helium enrichment but, by then, the stars have already left our O III–I sample.

The lower panel in Fig. 8 shows O-star tracks for an initial spin rate of approximately 300  $\text{km s}^{-1}$ . In this case, the Köhler et al. (2015) models do predict an increase in  $Y$  during the O star phase for initial masses  $\sim 60 M_{\odot}$  and up. Initially, they spin so fast that rotationally-induced mixing prevents the build-up of a steep chemical gradient at the core boundary. The lack of such a barrier explains the initial rise in  $Y$ . However, as a result of loss of angular momentum via the stellar wind and the associated spin-down of the star, a chemical gradient barrier may develop during its main-sequence evolution. Such a gradient effectively acts as a ‘wall’ inhibiting the transport of helium to the surface. This can

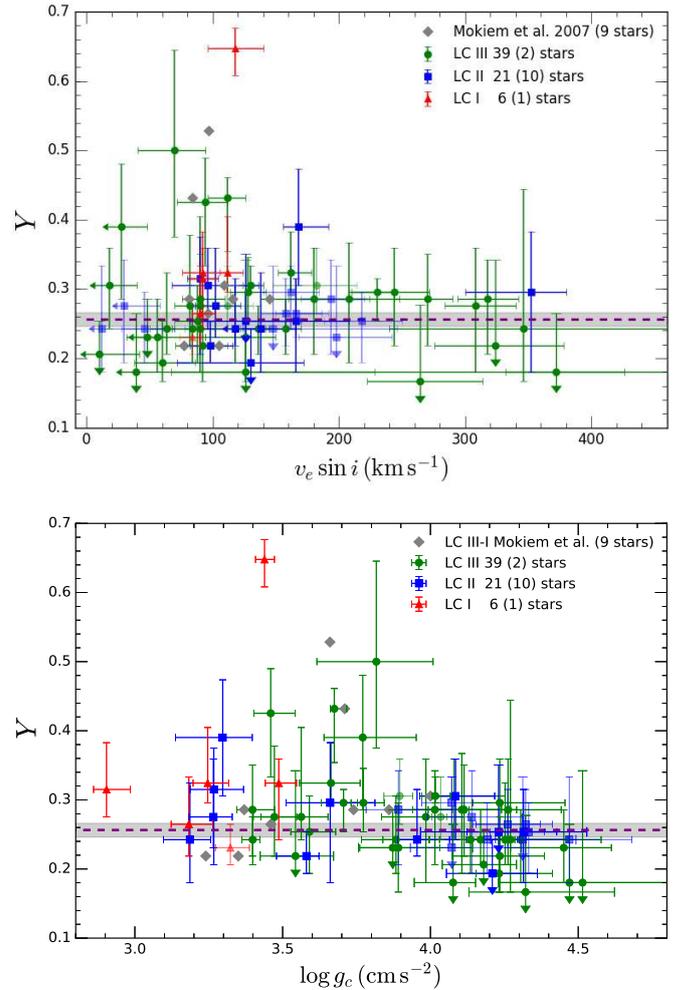


**Fig. 7.** Helium mass fraction  $Y$  versus  $v_e \sin i$  (upper panel) and  $\log g_c$  (lower panel). Symbols and colors have the same meaning as in Fig. 5. Gray diamonds denote stars with LC III to I from Mokiem et al. (2007a). The purple dashed line at  $Y = 0.255$  defines the initial composition for LMC stars; the gray bar is the  $3\sigma$  uncertainty in this number.

be seen in Fig. 8 as a flattening of the  $Y$  increase with time. Once such a barrier develops, the star starts to evolve to cooler temperatures, an evolution that was prohibited in the preceding phase of quasi-chemically homogeneous evolution. Once redward evolution commences, stripping of the envelope by mass loss may aid in increasing the surface helium abundance. In our tracks this is only significant for initial masses  $125 M_{\odot}$  and up.

Finally, our findings might indicate that the current implementation of rotational mixing and wind stripping in single-star models is not able to justify the  $Y$  abundances of most of the helium enriched stars in our sample. In the following subsection we combine the constraints on the helium abundance with the projected spin rate of the star and its position in the Hertzsprung-Russell diagram to further scrutinize the evolutionary models.

#### 4.4. Hertzsprung-Russell diagram

In this section, we explore the evolutionary status of our sample stars by means of the Hertzsprung-Russell diagram (see Fig. 9).

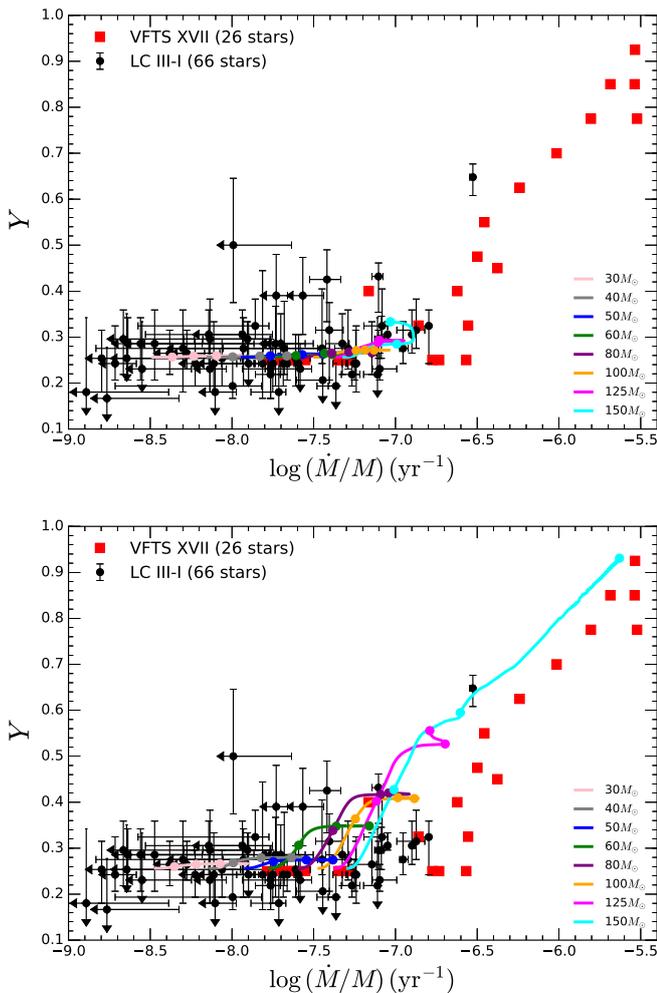


**Fig. 8.** Helium mass fraction  $Y$  versus the empirical (unclumped) mass-loss rate relative to the stellar mass ( $\dot{M}/M$ ) for our sample stars with their respective 95% confidence intervals. Added to this is the set of very massive luminous O, Of, Of/WN and WNh stars analyzed in Paper XVII, excluding the nine stars in common with this paper. Also shown are evolutionary tracks by Brott et al. (2011) and Köhler et al. (2015) for stars with initial spin rates of approximately  $200 \text{ km s}^{-1}$  (upper panel) and  $300 \text{ km s}^{-1}$  (lower panel) with dots every 1 Myr of evolution. These tracks are truncated at  $30 \text{ kK}$ , which is approximately the temperature where the stars evolve into B-type objects and thus are no longer part of our observational sample.

Two versions of the HRD are shown in Fig. 9. In the top panel, our sample of giants, bright giants, and supergiants is complemented with the VFTS samples of very massive stars (VMS) from Paper XVII and of LC V stars from Paper XIII. VMS populate the upper left part of the HRD. Giants, bright giants, and supergiants are predominantly located in between the 2 and 5 Myrs isochrones while dwarfs are found closer to the ZAMS. The location of LC V stars compared to III, II and I stars reflects their higher surface gravities as shown in Fig. 6. At the lowest luminosities, we note a predominance of LC III and II stars and an absence of LC V stars. As discussed in Sect. 4.2 this may reflect a classification issue.

The positions of the O stars in the HRD do not reveal an obvious preferred age but rather show a spread of ages, support-

ing findings of De Marchi et al. (2011), Cioni & the VMC team (2015), and Sabbi et al. (2015). HRDs of each of the spatial sub-populations defined in Sect. 2 do not point to preferred ages either (see Appendix B and Fig. B.1), suggesting that star formation has been sustained for the last 5 Myr at least throughout the Tarantula region. We stress that the central  $15''$  of Radcliffe 136, the core cluster of NGC 2070, is excluded from the VFTS sample. The age distribution of the Tarantula massive stars will be investigated in detail in a subsequent paper in the VFTS series (Schneider et al., in prep.).

In the lower panel of Fig. 9, we include information on  $Y$  and  $v_e \sin i$  for our sample stars. We also include iso-helium lines for  $Y = 0.30$  and  $0.35$  as a function of initial rotational velocity (see figure 10 of Köhler et al. 2015). According to these tracks, main-sequence stars initially less massive than  $\sim 100 M_\odot$  with initial rotation rates of  $200 \text{ km s}^{-1}$  or less are not expected to show significant helium surface enrichment, that is,  $Y < 0.30$ . Stars with an initial rotation rate of  $300 \text{ km s}^{-1}$  are only supposed to reach detectable helium enrichment in the O star phase if they are initially at least  $60 M_\odot$ . Helium enrichment is common for  $20 M_\odot$  stars and up if they spin extremely fast at birth ( $v_e > 400 \text{ km s}^{-1}$ ). Below we discuss how this compares with our sample stars.

First, our finding that all helium enriched stars have a present day projected spin rate of less than  $200 \text{ km s}^{-1}$  (see also Fig. 7) appears at odds with the predictions of the tracks referred to above. In the LMC, significant spin-down due to angular-momentum loss through the stellar wind and/or secular expansion is only expected by Brott et al. (2011) and Köhler et al. (2015) for stars initially more massive than  $\sim 40 M_\odot$ , once these objects evolve into early-B supergiants (Vink et al. 2010). Only for much higher initial mass are the winds sufficiently strong to cause rotational braking during the O-star phase. This could perhaps help explain the two highest-luminosity He-enriched objects, VFTS 180 and 518, though in the context of our models this requires an initial spin of  $400 \text{ km s}^{-1}$  and wind strengths typical for at least  $\sim 125 M_\odot$  stars. Their evolutionary masses are at most  $50 M_\odot$ . It is furthermore extremely unlikely that the remaining three He-enriched stars at lower luminosity (having initial masses  $< 40 M_\odot$ ) spin at  $400 \text{ km s}^{-1}$  and are all seen almost pole-on. For the two hot He-enriched stars VFTS 180 and 518 we included a set of nitrogen diagnostic lines (see Sect. 3.1). Interestingly, we find that they are nitrogen enriched as well (i.e.,  $[\text{N}] > 8.5$ ). A thorough nitrogen analysis of the full sample is presented by Grin et al. (2016, see also Summary).

If indeed these are main-sequence (core H-burning) stars that live their life in isolation, rotational mixing, as implemented in the evolutionary predictions employed here, cannot explain the surface helium mass fraction in this particular subset of stars. This would point to deficiencies in the physical treatment of mixing processes in the stellar interior.

Alternatively, the high helium abundances could point to a binary history (e.g., mass transfer or even merger events; see e.g., de Mink et al. 2014; Bestenlehner et al. 2014) or post-red supergiant (post-RSG) evolution. Concerning the former option, one of these sources is VFTS 399, which has been identified as an X-ray binary by Clark et al. (2015). Concerning the latter option, LMC evolutionary tracks that account for rotation and that cover the core-He burning phase have been computed by Meynet & Maeder (2005). These tracks indicate that a brief part of the evolution of stars initially more massive than  $25 M_\odot$  may be spent as post-RSG stars hotter than  $30\,000 \text{ K}$ . However, these exceptional stars would be close to the end of core-helium burning and feature much higher helium (and nitrogen) surface abundances.

Second, while we have only a few fast rotators, these stars do not seem to be helium enriched (see again Fig. 7). All of them have masses below  $20 M_{\odot}$ , therefore no significant helium enrichment is expected, in agreement with our measurements. If such fast rotators are spun-up secondaries resulting from binary interaction (e.g., Ramírez-Agudelo et al. 2013; de Mink et al. 2013), then the interaction process should have been helium neutral. Some of the stars appear to have sub-primordial helium abundances. This could also be an indication of present-day binarity (see Sect. 4.3). Among them are some of the fastest spinning objects, consistent with the latter conjecture.

#### 4.5. Mass loss and modified wind momentum

In the optical, the mass-loss rate determination relies on wind infilling in  $H\alpha$  and  $He\ II\ \lambda 4686$ . These recombination lines are indeed sensitive to the invariant wind-strength parameter  $Q = \dot{M}/(Rv_{\infty})^{3/2}$  that is inferred from the spectral analysis (see, e.g., Puls et al. 1996; de Koter et al. 1998). For approximately 40% of our sample only upper limits on  $\dot{M}$  can be determined. These stars mostly have  $\dot{M} < 10^{-7} M_{\odot}\text{yr}^{-1}$  and  $\log(L/L_{\odot}) < 5.0$ . This group of relatively modest-mass stars ( $M_{\text{spec}} \leq 25 M_{\odot}$ ) is excluded from the analysis presented in this section.

To facilitate a comparison of the mass-loss rates of the remaining stars with theoretical results, we use the modified wind momentum luminosity diagram (WLD; Fig. 10). The modified wind momentum  $D_{\text{mom}}$  is defined in Sect. 3.5. For a given metallicity,  $D_{\text{mom}}$  is predicted to be a power-law of the stellar luminosity, that is,

$$\log D_{\text{mom}} = x \log(L_{*}/L_{\odot}) + \log D_0, \quad (4)$$

where  $x$  is the inverse of the slope of the line-strength distribution function corrected for ionization effects (Puls et al. 2000). For a metal content of solar down to  $\sim 1/5$ th solar,  $x$  and  $D_0$  do not depend on spectral type for the parameter range considered here, which allows for a simple (i.e., power-law) prescription of the mass-loss metallicity dependence.

The top panel of Fig. 10 shows the WLD for our sample, where  $D_{\text{mom}}$  is in the usual units of  $\text{g cm s}^{-2}$ . Upper limits for the weak-wind stars are also shown (see legend). A linear fit to the stars for which we have a constraint on the mass-loss rate is given in blue, with the shaded blue area representing the uncertainty as a result of errors in  $D_{\text{mom}}$ . Also plotted in the figure are the results of Mokiem et al. (2007b) for 38 stars in total in the LMC (sub-)sample, 16 of which are in N11. Our results exhibit somewhat higher  $D_{\text{mom}}$  values than those of Mokiem et al. (2007b). The reason for this discrepancy is illustrated in the lower panel, where we have repeated our analysis applying identical fitting constraints as Mokiem et al. This implies that we let  $\beta$  be a free parameter and have removed the nitrogen lines from our set of diagnostics. In that case, we recover essentially the same result. As pointed out in Sect. 3.7, allowing the method to constrain the slope of the velocity law yields higher  $\beta$  values compared to the adopted values, that is, those based on theoretical considerations, for a substantial fraction of the stars. A shallower velocity stratification (that is, a higher  $\beta$ ) in the  $H\alpha$  and  $He\ II\ \lambda 4686$  forming regions corresponds to a higher density for the same  $\dot{M}$ . As the recombination lines depend on the square of the density, the emission will be stronger (at least in the central regions of the profile). Hence, to fit the profiles compared to a lower  $\beta$ , one needs to reduce the mass loss in the models.

When compared to the theoretical predictions of Vink et al. (2001), who apply the same prescription to estimate  $v_{\infty}$  as used

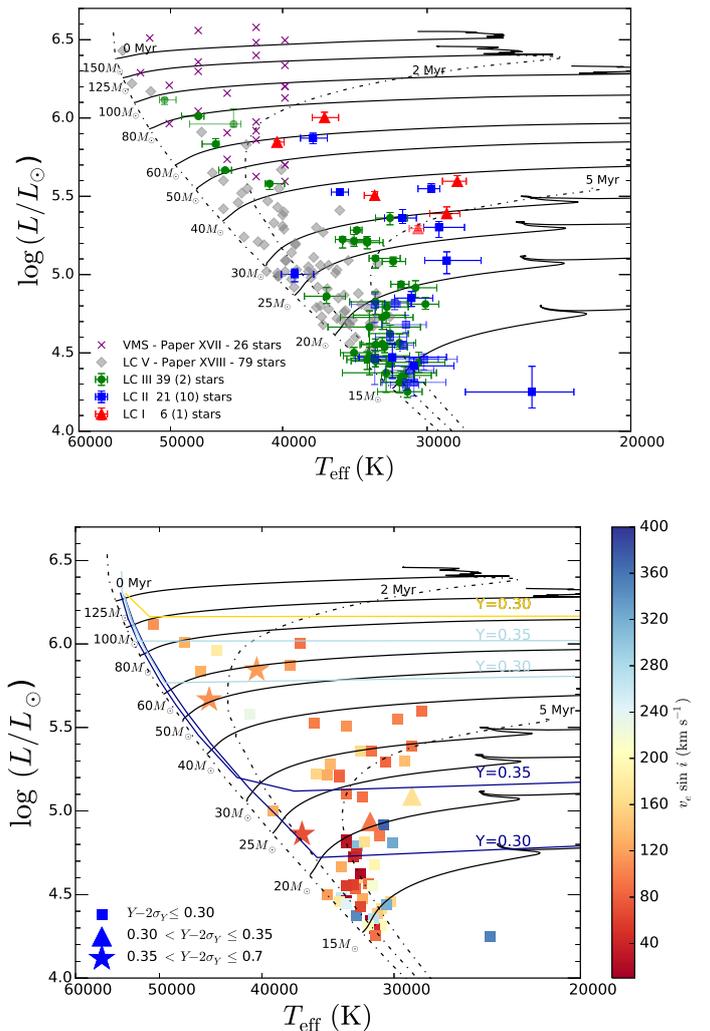


**Fig. 9.** Two versions of the Hertzsprung-Russell diagram. In the top panel our sample of single O-type giants and supergiants is supplemented with the dwarf O star sample of Paper XIII and the sample of very massive Of and WNh stars by Paper XVII. We exclude the results of Paper XVII for the nine stars in common with this paper and adopted our results (see Sect. 3.4.3). Symbols and colors have the same meaning as in Fig. 6. The lower panel only contains the sample studied here. The symbol shapes in the lower panel show three categories of helium mass fraction, that is, not enriched (squares), moderately enriched (triangles), and enriched (stars). The symbol colors refer to their projected rotational velocity (see color bar on the right). Evolutionary tracks and isochrones are for models that have an initial rotational velocity of approximately  $200 \text{ km s}^{-1}$  (Brott et al. 2011; Köhler et al. 2015). Iso-helium lines for different rotational velocities are from Köhler et al. (2015) and are color-coded using the color bar.

here (see Sect. 3.1), our strong-wind stars show higher  $D_{\text{mom}}$  values. This is interpreted as being due to inhomogeneities in the outflow, usually referred to as clumping. Empirical evidence for clumpy outflows has been presented by Eversberg et al. (1998), Lépine & Moffat (2008), and Prinja & Massa (2010), for example. If the winds are clumped, disregarding this effect would lead to an overestimation of the empirical  $H\alpha$  or  $He\ II\ \lambda 4686$ -based mass-loss rate by a factor of  $f_V^{-1/2}$ , where  $f_V$  is the clump

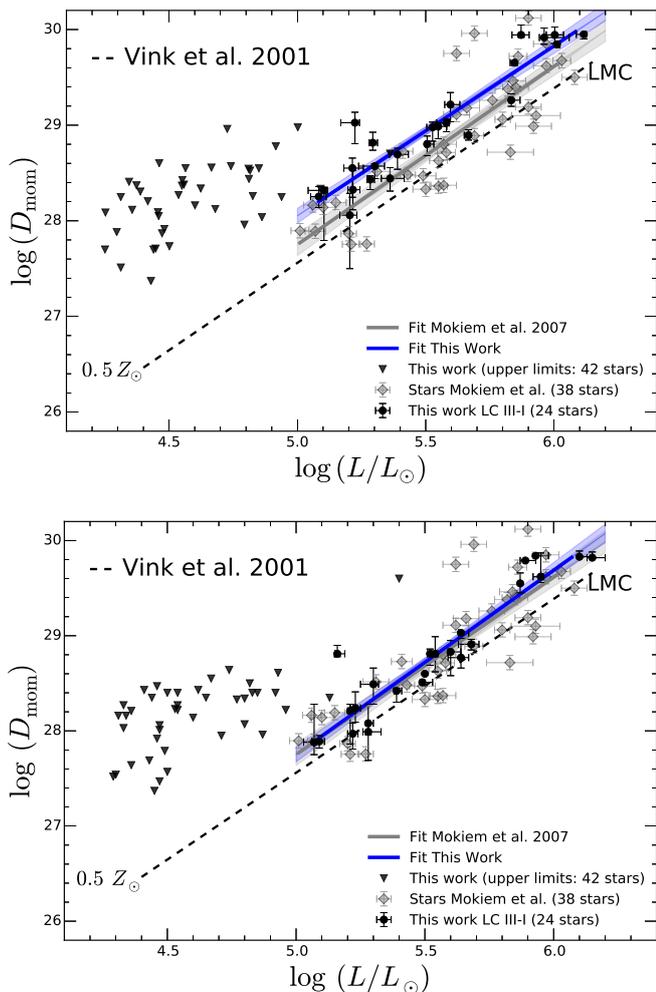


**Fig. 10.** Modified wind momentum ( $D_{\text{mom}}$ ) vs. luminosity diagram. The dashed lines indicate the theoretical predictions of Vink et al. (2001) for homogeneous winds. *Top panel*: the empirical fit for this work and Mokiemi et al. (2007a) (both for  $L/L_{\odot} > 5.0$ ) in shaded blue and gray bars, respectively. For stars with  $L/L_{\odot} \leq 5.0$ , only upper limits could be constrained. These stars are not considered in the analysis. *Bottom panel*: same as top panel but now for an analysis in which the acceleration of the wind flow,  $\beta$ , is a free parameter and in which the analysis does not include nitrogen lines, but relies on hydrogen and helium lines only. [Color version available online].

volume-filling factor. This assumes the clumps to be optically thin for the considered diagnostic lines, and the inter-clump medium to be void. To reconcile our results with theory would require  $f_V \sim 1/8$  to  $1/6$ , reducing the mass-loss rate by a factor of 2.8. This is a somewhat stronger reduction than implied by the volume-filling factors  $f_V \sim 1/2$  to  $1/3$  found by Mokiemi et al. (2007b), which correspond to a reduction in  $\dot{M}$  relative to a homogeneous outflow of approximately a factor of 1.5.

Placing constraints on the properties of the clumps in the  $H\alpha$  and  $\text{He II } \lambda 4686$ -forming region relies on the accuracy of the theoretical mass-loss rates but does not imply in any way that the Vink et al. (2001) predictions are correct. Critical assumptions in these theoretical results are that  $\dot{M}$  relies on a global energy conservation argument (see Abbott & Lucy 1985; de Koter et al. 1997) and that the outflow is homogeneous. For the strong-wind

**Table 3.** Coefficients describing empirical and theoretical modified-wind momentum relations.

Sample	Slope	Intercept
<i>Empirical</i>		
This work	$1.78 \pm 0.14$	$19.17 \pm 0.79$
Mokiemi et al. (2007b)	$1.87 \pm 0.19$	$18.30 \pm 1.04$
<i>Theoretical LMC relation</i>		
Vink et al. (2001)	$1.83 \pm 0.04$	$18.43 \pm 0.26$

stars investigated here, Muijres et al. (2012) showed that wind solutions based on a detailed treatment of the line force yielded mass-loss rates to within 0.1 dex when adopting the same terminal flow velocities, supporting the reliability of the global energy conservation assumption applied by Vink et al. (2001). If the material in the outflow would be concentrated in relatively few and strongly over-dense clumps, porosity effects may cause photons to escape ‘in-between the clumps’ reducing the line-driving force and hence the mass-loss rate (for corresponding scaling relations, see Sundqvist et al. 2014). However, Muijres et al. (2011) demonstrated that for clumps that are smaller than  $1/100$ th of the local density scale height, thought to represent physically realistic situations, such effects are not significant for volume-filling factors as low as approximately  $1/30$ .

As for the empirically derived filling factors, Massa et al. (2003) and Fullerton et al. (2006), by analyzing the  $P v \lambda 1118, 1128$  resonance line doublet, find cases where  $f_V$  reaches values as low as  $1/100$ , as does Najarro et al. (2011). Bouret et al. (2003, 2005, 2013) derive clumping properties from  $O v \lambda 1371$ , with a mode of  $1/10$  but also reporting extremely low volume-filling factors in some cases. Extending the original work from Oskinova et al. (2007) to 3D simulations, Šurlan et al. (2013) point out that the assumption of optically thin clumps breaks down for the phosphorous lines, showing that for a distribution of clump optical depths, a match to both the strength of  $P v$  and  $H\alpha$  is found for much larger  $f_V$ . These authors present such matches for an assumed  $f_V = 1/10$ , but we note that simultaneous fits may also be realised for somewhat larger filling factors. Sundqvist et al. (2010, 2011) compute stochastic wind models, allowing also for porosity in velocity space and a non-void interclump medium. For the case of  $\lambda$  Cep their results imply a mass-loss rate that is half of that predicted by Vink et al. (2001) and  $f_V$  values larger than  $1/30$ . Finally, for O stars brighter than  $L = 10^5 L_{\odot}$  a model independent mass-loss constraint that can be obtained from stars that have spectral morphologies in transition from Of to Wolf-Rayet type, that is, Of/WNh stars, points to volume-filling factor  $f_V \sim 1/10$  (Vink & Gräfenner 2012).

We conclude that the mass-loss rate predictions of Vink et al. (2001) for LMC metallicity are consistent with  $H\alpha$  and  $\text{He II } \lambda 4686$ -based wind volume-filling factors of  $f_V \sim 1/8$  to  $1/6$  and that such volume-filling factors appear to be in reasonable agreement with empirical constraints that rely on models that account for optical depth effects in the clumps and porosity of the wind medium.

#### 4.6. Mass discrepancy

The discourse on the mass discrepancy in massive stars, triggered by the work on Galactic stars by Groenewegen & Lamers (1989) and Herrero et al. (1992), is extensive and a general consensus on the topic is yet to be reached. If present, the discrepancy usually implies that evolutionary masses are found















































